

# ADOP: Approximate Differentiable One-Pixel Point Rendering

DARIUS RÜCKERT, Friedrich-Alexander-Universität Erlangen-Nürnberg, Germany

LINUS FRANKE and MARC STAMMINGER, Friedrich-Alexander-Universität Erlangen-Nürnberg, Germany

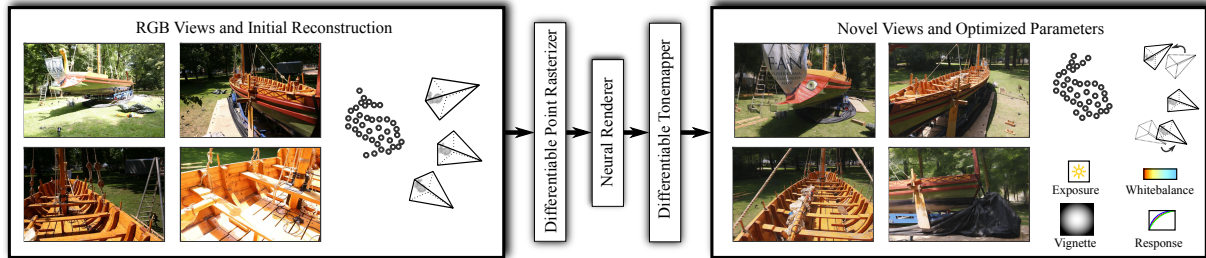


Fig. 1. Given a set of RGB images and an initial 3D reconstruction (left), our inverse rendering approach is able to synthesize novel frames and optimize the scene’s parameters (right), for instance point position and camera pose as well as image settings such as exposure time and white balance. In combination with a fast point-based renderer, we achieve real-time render times even for complex environments.

In this paper we present ADOP, a novel point-based, differentiable neural rendering pipeline. Like other neural renderers, our system takes as input calibrated camera images and a proxy geometry of the scene, in our case a point cloud. To generate a novel view, the point cloud is rasterized with learned feature vectors as colors and a deep neural network fills the remaining holes and shades each output pixel. The rasterizer renders points as one-pixel splats, which makes it very fast and allows us to compute gradients with respect to all relevant input parameters efficiently. Furthermore, our pipeline contains a fully differentiable physically-based photometric camera model, including exposure, white balance, and a camera response function. Following the idea of inverse rendering, we use our renderer to refine its input in order to reduce inconsistencies and optimize the quality of its output. In particular, we can optimize structural parameters like the camera pose, lens distortions, point positions and features, and a neural environment map, but also photometric parameters like camera response function, vignetting, and per-image exposure and white balance. Because our pipeline includes photometric parameters, e.g. exposure and camera response function, our system can smoothly handle input images with varying exposure and white balance, and generates high-dynamic range output. We show that due to the improved input, we can achieve high render quality, also for difficult input, e.g. with imperfect camera calibrations, inaccurate proxy geometry, or varying exposure. As a result, a simpler and thus faster deep neural network is sufficient for reconstruction. In combination with the fast point rasterization, ADOP achieves real-time rendering rates even for models with well over 100M points.

<https://github.com/darglein/ADOP>

CCS Concepts: • **Computing methodologies** → **Reconstruction; Rendering; Image-based rendering**; *Neural networks*.

Additional Key Words and Phrases: Image-based Rendering, Novel View Synthesis, Neural Rendering, Machine Learning, Inverse Rendering

Authors’ addresses: Darius Rückert, [darius.rueckert@fau.de](mailto:darius.rueckert@fau.de), Friedrich-Alexander-Universität Erlangen-Nürnberg, Erlangen, Germany; Linus Franke, [linus.franke@fau.de](mailto:linus.franke@fau.de); Marc Stamminger, [marc.stamminger@fau.de](mailto:marc.stamminger@fau.de), Friedrich-Alexander-Universität Erlangen-Nürnberg, Erlangen, Germany.

## 1 INTRODUCTION

With neural rendering it is possible to generate stunning free-viewpoint reconstructions of real world scenes. The field has advanced enormously in the last years with two major streams emerging [Tewari et al. 2020]: Proxy-based approaches that use some 3D proxy to carry reconstructed scene information (e.g., triangle meshes [Thies et al. 2019] or point clouds [Aliev et al. 2020]), and direct approaches that encode light or radiance fields (e.g., NeRFs [Mildenhall et al. 2020]).

Approaches with geometric proxies extend the idea of previous image based rendering methods [Chaurasia et al. 2013], with the difference that neural networks are used to interpolate and blend the input images on the geometric proxy. The rationale is that neural networks can achieve a better interpolation of view-dependent effects as well as handle imperfections of the geometric proxy and the resulting reprojection errors. Although this holds true to some degree, inconsistencies in the input still have significant impact on the quality of the result. As such, slight miscalibration of intrinsic and extrinsic camera parameters can lead to blurred results. Even worse, varying camera exposure in the input images cannot be compensated well and leads to patches of inconsistent brightness.

In this paper, we present a novel neural rendering system that directly accounts for such inconsistencies and renders very efficiently. As input we assume a number of images of a scene. A standard 3D reconstruction pipeline estimates intrinsic and extrinsic camera parameters and reconstructs a point cloud of the scene geometry. Following prior point-based neural rendering work [Aliev et al. 2020], we learn feature vectors for all points and generate novel views by rendering the point cloud to an image pyramid, from which a deep neural network generates the final image.

However, our renderer is differentiable with respect to structural input parameters, such as intrinsic and extrinsic camera parameters, camera exposure, and even point cloud positions. The core idea is an approximation of the spatial gradients of one-pixel point splatting, an otherwise non-differentiable operation. We thus call our method ADOP: Approximate differentiable one-pixel point rendering. Using

this technique, we can apply the idea of inverse rendering and use the renderer itself to improve its output by optimizing the input (see Fig. 1). In this paper, we show that this self-calibration reduces a large variety of sources of inconsistencies in the input, resulting in high-quality novel view synthesis, less constraints on the input, and faster rendering times.

In detail, ADOP makes the following contributions:

- We present a point-based rendering pipeline, that can self-optimize all structural input parameters obtained from the reconstruction, namely camera poses, lens distortions, and even point cloud positions, which leads to significantly improved render quality.
- We show how to optimize for camera response and vignetting, as well as per-image exposure and white balancing to support input images with varying exposure, as it is almost unavoidable for outdoor scenes. As a side effect, the learned features encode the scene texture in high-dynamic range, and it is possible to apply arbitrary tone mapping operators to the synthesized views.
- We present a highly efficient rasterizer and rendering optimizations with which our system achieves real-time rendering rates. We show that due to the significantly improved input, smaller networks are sufficient to achieve good rendering quality. Together with a highly optimized point renderer, we can render photo realistic full-HD images in 30FPS on off-the-shelf hardware.

## 2 RELATED WORK

### 2.1 Novel View Synthesis

Traditional novel view synthesis, which is closely related to image-based rendering (IBR), relies on the basic principle of warping colors from one frame to another. One approach is to use a triangle-mesh proxy to directly warp the image colors to a novel view [Chaurasia et al. 2013; Debevec et al. 1998; Shum and Kang 2000]. However, imperfect geometry leads to ghosting artifacts around silhouettes. This can be improved by replacing hand-crafted heuristics in the classic IBR pipeline with deep neural networks [Hedman et al. 2018; Riegler and Koltun 2020, 2021; Thies et al. 2020]. If no proxy geometry is available, learning-based approaches have been developed that create a multi plane image representation [Mildenhall et al. 2019; Srinivasan et al. 2019; Tucker and Snavely 2020; Zhou et al. 2018] or directly estimate the required warp-field [Flynn et al. 2016; Ganin et al. 2016; Zhou et al. 2016]. Novel view synthesis can also be performed by reconstructing a 3D model of the scene and rendering it from novel view points. Thies et al. [2019] learn a neural texture on a triangle mesh which can be rendered using traditional rasterization. The rasterized image is then converted to RGB by a deep neural network. Other approaches use ray-casting to automatically learn a voxel grid [Nguyen-Phuoc et al. 2018; Sitzmann et al. 2019; Zhu et al. 2018] or an implicit function [Mescheder et al. 2019; Park et al. 2019]. It has also been shown that point clouds are suitable geometric proxies for novel view synthesis [Meshry et al. 2019; Pittaluga et al. 2019]. *Neural Point-based Graphics* (NPBG) [Aliiev et al. 2020], which is closely related to our method, renders a point cloud with learned neural descriptors in multiple resolutions. These

images are then used to reconstruct the final output image by a deep neural network. NPBG is very flexible as it doesn't require a textured triangle mesh as proxy and shows impressive results. Similarly, Dai et al. [2020] show that rendering multiple depth layers of a point cloud can also be used to synthesize novel views.

### 2.2 Inverse Rendering

Inverse rendering and differentiable rendering have been a topic of research for some time. However, major breakthroughs have only been made in recent years due to improved hardware and advancements in deep learning [Kato et al. 2020]. Its application can be challenging though: Traditional triangle rasterization with depth-testing has no analytically correct spatial derivative [Kato et al. 2020; Loper and Black 2014]. Available systems therefore either approximate the gradient [Genova et al. 2018; Kato and Harada 2019; Kato et al. 2018; Loper and Black 2014] or approximate the rendering itself using alpha blending along edges [Chen et al. 2019; Liu et al. 2019a; Rhodin et al. 2015]. Volume raycasting on the other hand is differentiable by accumulating all voxel values along the ray [Kato et al. 2020]. This has been used by multiple authors to build volumetric reconstruction systems [Henzler et al. 2019; Lombardi et al. 2019; Tulsiani et al. 2017] or predict the signed distance field of an object [Jiang et al. 2020]. Instead of a voxel grid, an implicit function can also be used inside a differentiable volumetric raycasting framework [Liu et al. 2019b, 2020; Niemeyer et al. 2020; Zakharov et al. 2020]. Mildenhall et al. [2020] show with *Neural Radiance Fields* (NeRF) that a deep neural network can be trained by volumetric raycasting to store the view-dependent radiance of an object. Due to the impressive results of NeRF, multiple extensions and improvements have been published in the following years [Martin-Brualla et al. 2021; Sitzmann et al. 2020; Yu et al. 2021; Zhang et al. 2020]. Inverse rendering has also been proposed for point cloud rasterization [Kato et al. 2020; Lin et al. 2018]. The spatial gradients of the points can be approximated in different ways. This includes gradient computation along silhouettes [Han et al. 2020], gradients for Gaussian splatting [Kopanas et al. 2021; Wiles et al. 2020; Yifan et al. 2019], and gradient approximation using a temporary 3D volume [Insafutdinov and Dosovitskiy 2018]. A different approach is taken by Lassner and Zollhöfer [2021] who render the points as small spheres instead of splats. Our differentiable point rendering approach is similar to established differentiable splatting techniques [Kopanas et al. 2021; Yifan et al. 2019], however we render only one pixel per point, which allows our approach to be multiple magnitudes more efficient than competing methods [Lassner and Zollhöfer 2021]. A nice property of a differentiable rendering pipeline is that the camera parameters can be optimized during rendering. Lin et al. [2021] and Jeong et al. [2021] show that the camera model and camera pose can be optimized in the NeRF pipeline by providing a differentiable projection module. This allows to correct small errors in the initial calibration or even estimate the scene's geometry from scratch. Similar work focuses on synthesizing photometric correct views by storing linear HDR radiance values inside the NeRF. A fixed tonemapper [Mildenhall et al. 2021] or neural tonemapper [Huang et al. 2021] then converts the integrated HDR intensities to the LDR color space.

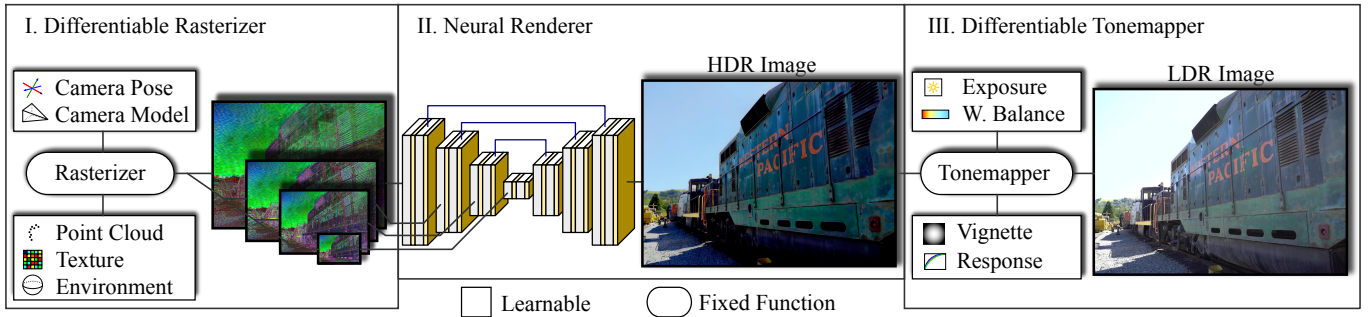


Fig. 2. Overview of our point-based HDR neural rendering pipeline. The scene, consisting of a textured point cloud and an environment map, is rasterized into a set of sparse neural images in multiple resolutions. A deep neural network reconstructs an HDR image, which is then converted to LDR by a differentiable physically-based tonemapper. All parameters in the rectangular boxes, as well as the neural network can be optimized simultaneously during training.

Concerning input refinement, this paper is inspired by these approaches and similar to concurrent work of Tancik et al. [2022]. However, we use an improved differentiable tonemapper module and apply the structural optimization on a point cloud instead of NeRFs.

### 2.3 Point-Based Rendering

Point-based rendering has been a topic of interest in computer graphics research for some time [Levoy and Whitted 1985]. Over the past decades two orthogonal approaches have been developed [Kobbelt and Botsch 2004]. The first major approach is the rendering of points as oriented discs, which are usually called *splats* or *surfels* [?], with the radius of each disc being precomputed from the point cloud density. To get rid of visible artifacts between neighboring splats, the discs are rendered with a Gaussian alpha-mask and then combined by a normalizing blend function [Alexa et al. 2004; Pfister et al. 2000; Zwicker et al. 2001]. Further extensions to surfel rendering exist, for example, Auto Splats, a technique to automatically compute oriented and sized splats [Preiner et al. 2012]. In recent years, deep learning-based approaches have been presented that improve image quality of surfel rendering, especially along sharp edges [Bui et al. 2018; Yang et al. 2020].

The second major approach to point-based graphics is point sample rendering [Grossman and Dally 1998], where points are rendered as one-pixel splats generating a sparse image of the scene. Using iterative [Rosenthal and Linsen 2008] or pyramid-based [Grossman and Dally 1998; Marroquim et al. 2007; Pintus et al. 2011] hole-filling approaches, the final image is reconstructed as a post processing step. To reduce aliasing in moving scenes, points with a similar depth value can be blended during rendering [Botsch et al. 2005; Schütz et al. 2021]. It has been shown that software implementations [Günther et al. 2013; Schütz et al. 2021] outperform hardware accelerated rendering through GL\_POINTS [Shreiner et al. 2009]. Recently developed approaches replace traditional hole-filling techniques with deep neural networks to reduce blurriness and better complete large holes [Le et al. 2020; Meshry et al. 2019; Pittaluga et al. 2019; Song et al. 2020].

## 3 NEURAL RENDERING PIPELINE

An overview of our end-to-end trainable neural rendering pipeline is shown in Fig. 2. As input, we use a point cloud, which can come from common Multiview Stereo or LiDAR and SLAM systems, and the novel frame’s camera parameters. Learned neural descriptors are assigned to the point cloud.

The first step in the pipeline is a differentiable *rasterizer* (Fig. 2 left), that renders each point as a one-pixel-sized splat by projecting it to image space using the camera parameters. Second, a deep *neural renderer* network is used to fill in holes and shade the image. Finally, a learnable *tone mapping* operator with a camera sensor model is applied, which converts the rendered high-dynamic range (HDR) image to the displayable low dynamic range (LDR). For optimization, input views are re-rendered, compared to the ground truth, and the loss is backpropagated through our rendering pipeline. Since all steps are differentiable, we can simultaneously optimize all parameters, in particular the scene structure, photometric model, point features, and network parameters, which improves consistency of the input and adds robustness from a possible imperfect reconstruction or calibration. In the following section, we detail on these three steps.

### 3.1 Differentiable One-Pixel Point Rasterization

*Forward Pass.* Our differentiable rasterizer renders multiple resolutions of a textured point cloud using one-pixel-sized splats. Formally speaking, the resolution layer  $l \in \{0, 1, \dots, L-1\}$  of the neural image  $I$  is the output of the render function  $\Phi_l$

$$I_l = \Phi_l(C, R, t, x, n, E, \tau), \quad (1)$$

where  $C$  is the camera model,  $(R, t)$  the camera pose,  $x$  the point position,  $n$  the point normal,  $E$  the environment map, and  $\tau$  the neural texture.

The rasterizer performs three steps, which are projection, occlusion check, and blending. The first step is the projection of each world point  $x$  into the image-space of layer  $l$ . Using the camera model  $C$  and the rigid transformation from world to camera-space  $(R, t)$ , we define this projection as:

$$P_l(C, R, t, x) = \frac{1}{2^l} C(Rx + t) \quad (2)$$



Fig. 3. One-pixel point rendering with fuzzy depth testing and threshold  $\alpha = 0$  on the left and  $\alpha = 0.01$  on the right.

The real valued result of  $P$  is then converted to pixel coordinates by rounding it to the nearest integer. A world point  $x_i \in \mathbb{R}^3$  is therefore projected to pixel coordinates  $p_i \in \mathbb{Z}^2$  by

$$p_i = \left\lfloor P_l(C, R, t, x_i) \right\rfloor. \quad (3)$$

Note that the rounding operation makes the projection discrete, which requires us to approximate its derivative (see later). After all points have been projected to image space, we discard them if they fail at least one of the following conditions:

$$\text{Bounds Test: } p_{ix} \in [0, w[ \quad \wedge \quad p_{iy} \in [0, h[ \quad (4)$$

$$\text{Normal Culling: } (Rn_i)^T \cdot \frac{Rx_i + t}{|Rx_i + t|} > 0 \quad (5)$$

$$\text{Depth Test: } z \leq (1 + \alpha) \min_z(p_i) \quad (6)$$

The last condition (6) is the fuzzy depth-test as described in Schütz et al. [2021]. A point passes the fuzzy depth test if its  $z$ -value is smaller than or equal to the scaled minimum depth value at that pixel. If the camera model does not provide a valid  $z$ -value, we instead use the distance between the camera and the 3D point. A large value of  $\alpha$  in Eq. (6) increases the number of points that pass the depth test. This leads to a smooth image but also can introduce artifacts when background points are merged into the foreground. In practice we use  $\alpha = 0.01$  as suggested by Schütz et al. [2021].

After the bounds check (4), normal culling (5), and fuzzy depth-test (6), for each pixel  $(l, u, v)$  we obtain a list of points  $\Lambda_{l,u,v}$ . If a pixel is not hit by any point, we sample the output color from the environment map  $E$  using the inverse camera projection  $C^{-1}$ . Otherwise, we sample the texture  $\tau$  of every point and write the mean into the output image. The blending function  $B_l$  can therefore be written as:

$$I_l(u, v, \Lambda) = \begin{cases} E(R^T C^{-1}(u, v)) & \Lambda_{l,u,v} = \emptyset \\ \frac{1}{|\Lambda_{l,u,v}|} \sum_{p \in \Lambda_{l,u,v}} \tau(p) & \text{else} \end{cases} \quad (7)$$

Fig. 3 shows two color images that have been rendered using the one-pixel point rasterization technique described in this section. We can see that with  $\alpha = 0.01$  (right image) the aliasing is significantly reduced and for example the letters are easier to read.

*Environment Map.* To represent the environment, we place a spherical environment map of resolution  $1024^2$  around the scene. Analog to the scene points, the environment map contains neural features, which are rendered as background. Both, the features of the point cloud and those of the environment map are learned using derivatives computed in the following backward pass.

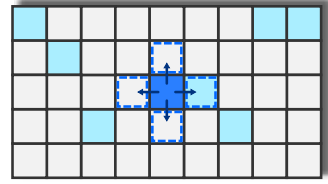


Fig. 4. Pixel lookup for the spatial gradient computation of the center (dark blue) point. The white pixels are from the background and the teal pixels are other rasterized points.

*Backward Pass.* The backward pass of our point rasterizer first computes the partial derivatives of the render function (1) w.r.t. its parameters.

$$\frac{\delta \Phi}{\delta C}, \frac{\delta \Phi}{\delta R}, \dots \quad (8)$$

Using the chain rule, we can then compute the parameter's gradient w.r.t. the loss and pass it to the optimizer. The difficult part of this calculation are the partial derivatives of the structural parameters  $C, R, t$  and  $x$ . This will be explained in the following section. The derivatives of the texture  $\tau$  and environment map  $E$  are straightforward and will not be detailed in this work.

The problem of deriving  $\Phi$  w.r.t. the structural parameters is the rounding operation Eq. (3) of our one-pixel point rasterizer. Due to the blending operation (7), it is not possible to compute the change of a pixel's color by moving a point out of this pixel, without storing a list of points with each pixel and reevaluating the blending function. So instead, we use an approximation that works well in practice. The principle is shown in Fig. 4. We virtually shift the projected point at  $p = (u, v)$  one pixel in each direction and compute the change of intensity *at the target pixels*, which is possible if we know the depth value at the target pixel. The induced intensity change of these shifts are:

$$\left. \frac{\Delta I}{\Delta u} \right|_{p=(u+1,v)}, \quad \left. \frac{\Delta I}{\Delta u} \right|_{p=(u-1,v)}, \quad \dots \quad (9)$$

from which we can approximate the gradient for  $u$  (equally for  $v$ ) at the desired location with

$$\left. \frac{\partial I}{\partial u} \right|_{p=(u,v)} \approx \frac{1}{2} \left( \left. \frac{\Delta I}{\Delta u} \right|_{p=(u-1,v)} + \left. \frac{\Delta I}{\Delta u} \right|_{p=(u+1,v)} \right). \quad (10)$$

To compute each induced change of (9), multiple cases have to be considered. As shown in Fig. 4, neighboring elements of  $p$  can either show a color from the environment map (background) or from other rasterized points. In the first case, the point simply overwrites the background, otherwise, three different cases have to be considered. Firstly, the virtually shifted point can be completely behind the neighbor in which case no intensity change would be induced. Secondly, the shifted point can be in front of the neighbor replacing the old color with the point's texture. Lastly, the neighbor point can have a similar depth value according to the fuzzy depth test (6), which causes us to have to compute the change of the blend function (7) if  $p$  is added to the neighboring  $\Lambda$ . In summary, the four cases to compute local spatial gradients are (with  $(i, j) =$

$(u \pm 1, v \pm 1)$ ):

$$\frac{\Delta I}{\Delta u} \Big|_{p=(i,j)} = \begin{cases} \tau(u, v) - I_l(i, j) & \Lambda_{l,u,v} = \emptyset \\ 0 & z > (1 + \alpha) \min_z(u, v) \\ \tau(u, v) - I_l(i, j) & z(1 + \alpha) < \min_z(u, v) \\ \frac{|\Lambda_{i,j}| I_l(i, j) + \tau(u, v)}{1 + |\Lambda_{i,j}|} - I_l(i, j) & \text{else} \end{cases} \quad (11)$$

*Stochastic Point Discarding.* Especially at small resolution layers, hundreds of points can pass the fuzzy depth-test of a single pixel, resulting in dramatic overdraw. To reduce this number, we apply a stochastic point-discarding technique similar to Enderton et al. [2010]. In a preprocess, we compute the world-space radius  $r_{world}$  as the distance to the 4th-nearest point. This radius is projected into screen-space during rendering, giving an approximation of the circular splat-size  $r_{screen}$ . Based on this size we then discard points stochastically to obtain a desired number of points per pixel by assigning each point a uniform random value  $\beta \in [0, 1]$  and rendering it only if the following condition is met:

$$\frac{r_{screen}}{\sqrt{1 - \beta}} > \frac{1}{\gamma} \quad (12)$$

The parameter  $\gamma$  roughly controls how many points are rendered per pixel. In our experiments, we use  $\gamma = 1.5$  for all datasets and scenes, see also Fig. 9.

*Implementation Details.* To implement the forward pass efficiently, we mainly follow the work of Schütz et al. [2021]. They propose a three-pass point rasterizer that outperforms traditional point rendering with GL\_POINTS. After a depth-only render pass, the color is accumulated for all points that pass the fuzzy depth-test. During accumulation, we track the number of points per pixel so we can compute Eq. (7) without writing the set  $\Lambda_{u,v}$  to memory. To further improve efficiency, we adopted the proposed blocked-morton-shuffle on the point cloud and use optimized local reductions inside the rasterization kernels. A side-effect of not explicitly storing  $\Lambda_{u,v}$  is that during backpropagation all points have to be rendered again. However, this re-rendering only marginally impacts performance as the total backpropagation time is dominated by the neural networks.

To further improve the pose estimation of our inverse rendering pipeline, we follow state-of-the-art SLAM systems [Engel et al. 2017; Mur-Artal and Tardós 2017; Rückert and Stamminger 2021] that optimize the rigid transformation  $(R, t) \in SE(3)$  in tangent-space. Linearized pose increments are expressed as the Lie-algebra elements  $x \in \mathfrak{se}(3)$  and applied to a transformation by

$$(R', t') = \exp(x) \cdot (R, t), \quad (13)$$

where  $\exp(x)$  is the exponential map from  $\mathfrak{se}(3)$  to  $SE(3)$ . To implement tangent-space optimization in libTorch [Jia et al. 2014][Paszke et al. 2019], we create a tangent tensor for the pose which is updated by the optimizer. After each step, the tangent is applied to the original pose (13) and reset to zero.

### 3.2 Neural Renderer

The neural renderer step (Fig. 2 center) uses the multi-resolution neural images to produce a single HDR output image. It consists

of a four layer fully convolutional U-Net with skip-connections, where the lower resolution input images are concatenated to the intermediate feature tensors. Downsampling is performed using average-pooling and the images are upsampled by bilinear interpolation. As convolution primitives, we use *gated convolutions* [Yu et al. 2019] which have been initially developed for hole-filling tasks and are therefore well suited for sparse point input. Overall the network architecture is similar to Aliev et al. [2020] with one less layer (see Sec. 4.6) and a few modifications to enable HDR imaging. First, we remove the batch-normalization layers, as they normalize the mean and standard deviation of intermediate images to fixed values. The total sensor irradiance is therefore lost and cannot be propagated from a 3D point to the final image. Usually, we store the neural point descriptors linearly, but if the scene’s radiance range is sizable (larger than 1 : 400) we use a logarithmic scaling, otherwise convergence issues with the optimizer can occur. For logarithmic descriptors, we convert them to linear space during rasterization so that the convolution operations only use linear brightness values.

### 3.3 Differentiable Tone Mapping

The HDR output image of the neural renderer is converted to LDR by a learnable tone mapping operator (Fig. 2 right), that mimics the physical lens and sensor properties of digital photo cameras. The first tone mapping stage applies brightness correction to the HDR image  $I_{HDR}$  using the estimated exposure value  $EV_i$  of image  $i$ .

$$I_e = \frac{I_{HDR}}{2^{EV_i}} \quad (14)$$

If image meta information is available, we initialize  $EV_i$  using Eq. (15), where  $f$  is the f-number of the optical system,  $t$  the exposure time in seconds,  $S$  the ISO arithmetic speed rating, and  $\overline{EV}$  the mean exposure value of all images. Otherwise, we initialize  $EV_i$  to zero for all images.

$$EV_i = \log_2 \left( \frac{f_i^2}{t_i} \right) + \log_2 \left( \frac{S_i}{100} \right) - \overline{EV} \quad (15)$$

After brightness correction, we compensate for a changing white balance by estimating the white point  $(R_i^w, G_i^w, B_i^w)$  for each image. During optimization, we keep  $G_i^w$  constant so that the white point cannot change the total image brightness.

As a next step, we model the *vignette* effect of digital cameras, which is a radial intensity falloff due to various optical and sensor-specific effects. The model we use [Goldman 2010] is a polynomial of the distance  $r$  of a pixel  $p$  to the vignette center  $c_v$ :

$$I_v = I_w \cdot (1 + a_2 r^2 + a_4 r^4 + a_6 r^6) \quad (16)$$

For better stability, we normalize  $p$  and  $c_v$  to be in the range  $[0, 1]$ . The coefficients  $a_i$  are initialized to zero and  $c_v$  is initialized to the image center.

The last stage in the tone mapping operator maps the linear RGB values to non-linear image intensities by applying the camera response function (CRF) [Grossberg and Nayar 2003] and an optional color space conversion from RGB to sRGB. We combine both operations into a single function  $R$ , which is implemented using a 1D texture for every color channel.

$$I_{ldr} = R(I_v) \quad (17)$$

Scene	#Points	#Images	Resolution	Exposure	White Balance	Camera Model	Initial Reconstruction
M60	9,713,277	313	2048 × 1080	Constant	Constant	Pinhole + Dist.	COLMAP
Train	11,818,812	301	1920 × 1080	Auto	Constant	Pinhole + Dist.	COLMAP
Playground	12,521,941	307	1920 × 1080	Auto	Constant	Pinhole + Dist.	COLMAP
Lighthouse	12,313,620	309	2048 × 1080	Auto	Constant	Pinhole + Dist.	COLMAP
Kemenate	34,144,401	405	2880 × 1920	Constant	Constant	Pinhole + Dist.	Metashape
Boat	53,036,216	742	2880 × 1920	Auto	Constant	Pinhole + Dist.	COLMAP
Office	72,916,173	688	5472 × 3648	Auto	Auto	Fisheye	LiDAR + SLAM

Table 1. Overview of our evaluation scenes. *M60*, *Train*, *Playground*, and *Lighthouse* are from the Tanks and Temples dataset. *Kemenate* and *Boat* were captured by the authors, *Office* was provided by (anonymous).

To guide the optimization towards a plausible response function, we initialize  $R(x)$  to  $x^{0.45}$  and add the following additional constraints based on Debevec and Malik [2008]:  $R(0) = 0$ ,  $R(1) = 1$ ,  $R''(x) = 0$ . These constraints ensure that the whole intensity range is covered and the response function is smooth. Overexposed and underexposed pixels are clamped to the maximum and minimum output values of 1 and 0. However, depending on the random network initialization, it is possible that the whole image is over/under exposed generating a zero gradient over the complete image. Inspired by the LeakyReLU activation function [Xu et al. 2015], we define a separate response function  $R_t$  during training that leaks small values instead of clamping them.

$$R_t(x) = \begin{cases} \alpha x & x < 0 \\ R(x) & 0 \leq x \leq 1 \\ \frac{-\alpha}{\sqrt{x}} + \alpha + 1 & 1 < x \end{cases} \quad (18)$$

The last term of Eq. (18) asserts that the maximum leaked value is  $(1+\alpha)$ . This is important in HDR scenes, because an overexposure of multiple magnitudes should not create a large gradient. In practice we use  $\alpha = 0.01$ , which results in a maximum image intensity of  $R_t(\infty) = 1.01$ .

## 4 EXPERIMENTS

### 4.1 Datasets and Evaluation Methodology

We have collected seven datasets with differences in size, modality, and camera settings (see Tab. 1). The first four scenes, i.e. *M60*, *Train*, *Playground*, and *Lighthouse*, are from the popular tanks and temples dataset [Knapitsch et al. 2017]. They consist of around 310 images in Full-HD resolution captured by a high-end video camera. We use COLMAP [Schönberger and Frahm 2016] to reconstruct the initial dense point-cloud as well as the camera extrinsics and intrinsics. The three remaining scenes, *Kemenate*, *Boat*, and *Office*, are added to show how ADOP can handle different capture setups as well as to evaluate some specific aspects of our pipeline. The *Boat* scene was captured outdoors with a large variance in exposure time. The *Office* dataset consists of very high resolution fisheye input images and its point cloud was produced by a LiDAR scanner instead of a multi-view stereo approach. For *Kemenate*, the initial reconstruction was processed by Metashape [Agisoft 2021]. Please see also the accompanying video for results of all scenes. As shown in Table 1, several scenes were captures with varying exposure, though

	Inference (RTX 3080)	Training (A100)
Nerf++	~ 183,000 ms	~ 24 h
SVS	~ 2,400 ms	> 48 h
NPBG	50 ms	~ 3 h
ADOP (ours)	<b>27 ms</b>	~ 4 h

Table 2. Timings for novel view synthesis averaged over the four tanks and temples scenes, and approximate training times. For SVS and Nerf++ we used the provided standard parameters for training.

only in *Boat* the exact exposure value is stored in the meta data. In the other cases, we let ADOP estimate the real exposure value for each image.

For a quantitative evaluation we follow the standard approach in our community. All input images are divided into a training set and a test set. The training set is used to optimize all parameters of our rendering pipeline over multiple epochs. We then let our system synthesize each test image and compare it to the real image using different metrics. Since the test images are also prone to miscalibration, we do a realignment and exposure estimation of the test images after training has been completed. For a fair comparison, we show the results with and without test refinement during our comparison to other approaches (see Tab. 4).

### 4.2 Training Details and Timings

Our inverse rendering pipeline (see Figure 2) is optimized end-to-end using the C++ front-end of libTorch. The neural network and the 4-element point descriptors are initialized randomly and optimized using ADAM [Kingma and Ba 2015] with an initial learning rate of 0.0002 and 0.08, respectively. If the radiance variation is high (see Sec. 4.11), the descriptors are stored logarithmically and their learning rate is reduced by a factor of 10. The remaining parameters, for example, camera pose and exposure time are updated using the SGD optimizer. Over time, each learning rate is reduced when a plateau is detected. For the exact values the reader is referred to the configuration files provided in the source code. To further improve the robustness of our pipeline, we delay the optimization of structural parameters and photometric parameters for 25 epochs. At that point, the rendered image is a blurry version of the target image and spatial gradients contain reasonable values.

	Train		Playground		M60		Lighthouse		Kemenate		Boat		Office	
	VGG ↓	Diff												
Baseline	514.3		374.8		369.5		508.5		204.7		652.9		186.8	
+ Env.	490.8	-5%	374.8	0%	364.1	-2%	440.1	-14%	202.5	-1%	646.1	-1%	185.5	-1%
+ Env. + TM	412.0	-19%	352.2	-6%	360.3	-3%	381.1	-25%	189.3	-8%	555.7	-15%	145.4	-22%
+ Env. + TM + SO	<b>368.1</b>	<b>-28%</b>	<b>318.7</b>	<b>-15%</b>	<b>317.7</b>	<b>-14%</b>	<b>350.0</b>	<b>-31%</b>	<b>180.2</b>	<b>-12%</b>	<b>535.6</b>	<b>-18%</b>	<b>131.7</b>	<b>-30%</b>

Table 3. Quantitative ablation study on the major contributions of ADOP. The improvements due to the environment map (Env), the tone mapper (TM), and the structure optimization (SO) differs between the scenes. For example, the M60 scene was captured with fixed exposure hence the tone mapper only has a small impact. The structure optimization is beneficial in all cases. A qualitative evaluation for the Train scene is shown in Figure 6.

	L1 ↓	MSE ↓	VGG ↓	PSNR ↑	LPIPS ↓	SSIM ↑
Train w. L1	<b>0.029</b>	<b>0.0033</b>	487.43	<b>25.10</b>	0.264	<b>0.846</b>
Train w. MSE	0.034	0.0037	558.84	24.67	0.322	0.822
Train w. VGG	0.032	0.0035	<b>357.08</b>	24.79	<b>0.145</b>	0.804

Fig. 5. Effect of training ADOP with different loss functions. Using the VGG loss for training improves the image quality significantly even though some metrics favor a training with L1 loss.

The training for all scenes was done on an NVidia A100 with 40GB video ram. The batch size was set to 16 with a crop size of  $512 \times 512$  pixels. The four tanks and temples scenes were trained for 400 epochs, which takes around 3.5 hours per scene. The remaining scenes were trained for 800 epochs. Table 2 shows an inference and training time comparison of ADOP to Nerf++, SVS and NPBG. Our method trains slightly slower than NPBG, mostly due to our more complex backpropagation, but still substantially faster than Nerf++ and SVS. At inference time, our method is the fastest and achieves real-time performance (<33ms) on an NVidia RTX3080.

### 4.3 Loss Function

We have trained ADOP on the M60 scene using typical loss functions also used in prior work: L1, MSE, and the VGG perceptual loss [Johnson et al. 2016]. For evaluation we use the LPIPS loss [Zhang et al. 2018], the peak signal-to-noise ratio (PSNR), and the structured similarity index (SSIM). The results are shown in Fig. 5. Using the VGG loss, the most details are visible and the overall sharpness is significantly improved compared to the other losses. All further experiments thus use VGG as loss function.



Fig. 6. Qualitative ablation study of the results presented in Table 3.

### 4.4 Ablation Study

Compared to previous work of neural point-based rendering, we have proposed several ideas to improve the quality of novel view synthesis. In Tab. 3 and Fig. 6, we analyze how much each module contributes to the final result. The first row shows a baseline experiment, which is similar to NPBG [Aliev et al. 2020]. After that we enable one by one, the environment map (Env), the tone mapper (TM), and the structure optimization (SO). In the latter, we initialize the scene using the COLMAP reconstruction and then optimize the camera pose, camera model, and point cloud during the training stage. All together, a significant improvement in image quality is achieved with a VGG loss reduction between 12% and 30%. The impact of the individual modules differs between the scenes. The indoor scenes (M60, Kemenate, and Office) are not improved by the environment map. The tonemapper shows the largest impact on scenes with a high variance in exposure times (Train, Lighthouse, Boat, Office). However, structure optimization yields a positive change on all datasets.

### 4.5 Robust Pose Correction

To further prove the robustness of our approximate gradient computation (see Sec. 3.1), we add Gaussian noise to the camera position and rotation. As shown in Fig. 7, ADOP is robust to a bad initial

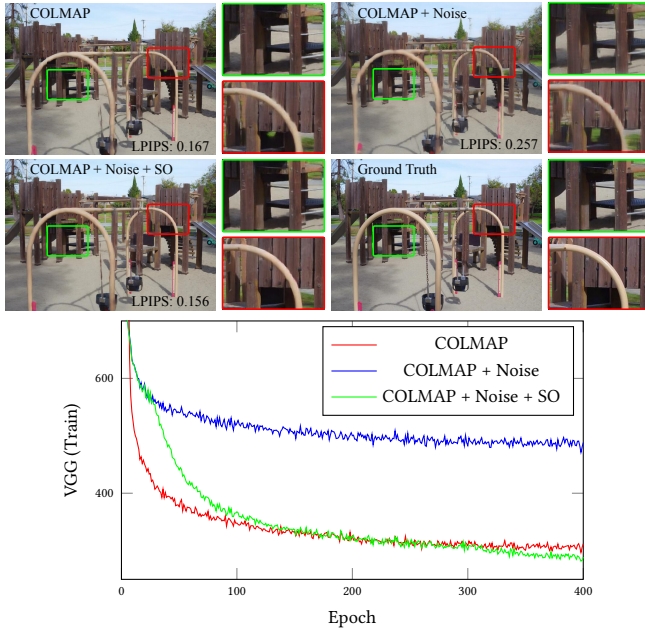


Fig. 7. Without structure optimization (SO), neural point-based rendering is sensitive to a bad initialization resulting in severe image artifacts (top right). However, our SO technique (bottom left) can recover from the erroneous input and outperforms the COLMAP initialization after 400 training epochs.

calibration and can also be used for image to point cloud alignment (see the supplemental material).

#### 4.6 U-Net Layers

Due to the improved consistency of the input, we can afford to use a smaller and faster neural network for final reconstruction. While other methods often use a five layer network [Aliev et al. 2020; Thies et al. 2019], we show in Fig. 8 that also fewer layers can produce good results. Note that with the number of layers in particular the hole-filling capabilities decrease, so that the chosen number of layers should be selected according to the point densities. In our experiments, we found that a four layer network improves efficiency and is less prone to overfitting, all shown results thus were generated with four layers.

#### 4.7 Stochastic Point Discarding

In Sec. 3.1 we proposed a stochastic point discarding technique to reduce the pixel overdraw. To examine a possible quality loss, we train ADOP with and without point discarding on the *Kemenate* dataset. We measure the number of blending operations, render time, and image quality, the result is presented in Fig. 9. Visually, no difference is noticeable, which is backed by the perceptual rendering loss. However, on average only 50% of the points are blended, which reduces rendering time by 20%.

#### 4.8 Comparison With Prior Work

We evaluate our system with state-of-the-art prior work on the scenes from the tanks and temples dataset [Knapitsch et al. 2017],

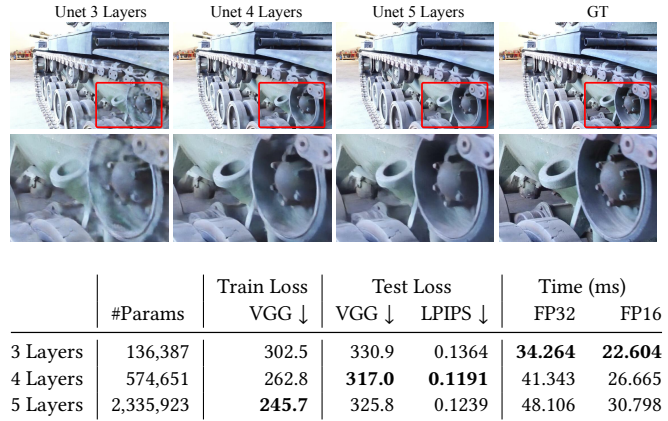


Fig. 8. Quality comparison on the number of Unet-layers inside the neural renderer. More layers improves the hole-filling capabilities (see images) but also reduces rendering efficiency. On some scenes, a 5 layer network is also prone to overfit on the training images (low train loss, but high test loss).

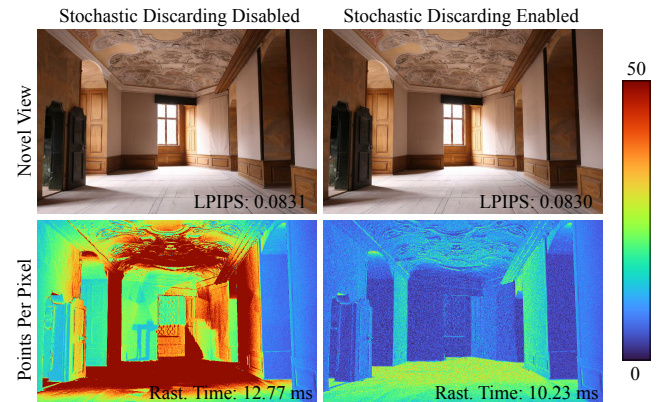


Fig. 9. Stochastic discarding roughly halves the number of blended points, which increases rasterization efficiency by 15-25%, without impact on quality.

see Tab. 1. The methods we compare against are SynSin [Wiles et al. 2020], Pulsar [Lassner and Zollhöfer 2021], Neural Rendering in the Wild (NRW) [Meshry et al. 2019], NeRF++ [Zhang et al. 2020], Stable View Synthesis (SVS) [Riegler and Koltun 2021], and Neural Point Based Graphics (NPBG) [Aliev et al. 2020]. The first two are general differentiable rendering front-ends that have been adapted by us to the novel view synthesis problem. They can be seen as similar to our approach and NPBG with the difference of using sphere and splat-based rendering instead of multi-resolution one-pixel point rendering. We did not compare against all related inverse rendering systems, because some are not applicable to our data [Loper and Black 2014] and others are outperformed by Pulsar and Synsin [Kato et al. 2020; Lin et al. 2018; Liu et al. 2019a].

Pulsar, Synsin, Nerf++ and SVS only support pinhole cameras. Therefore we train them on the undistorted images and camera parameters provided by COLMAP. During evaluation the synthesized undistorted images are distorted again and compared to the ground truth. NPBG, NRW, and our approach use one-pixel point

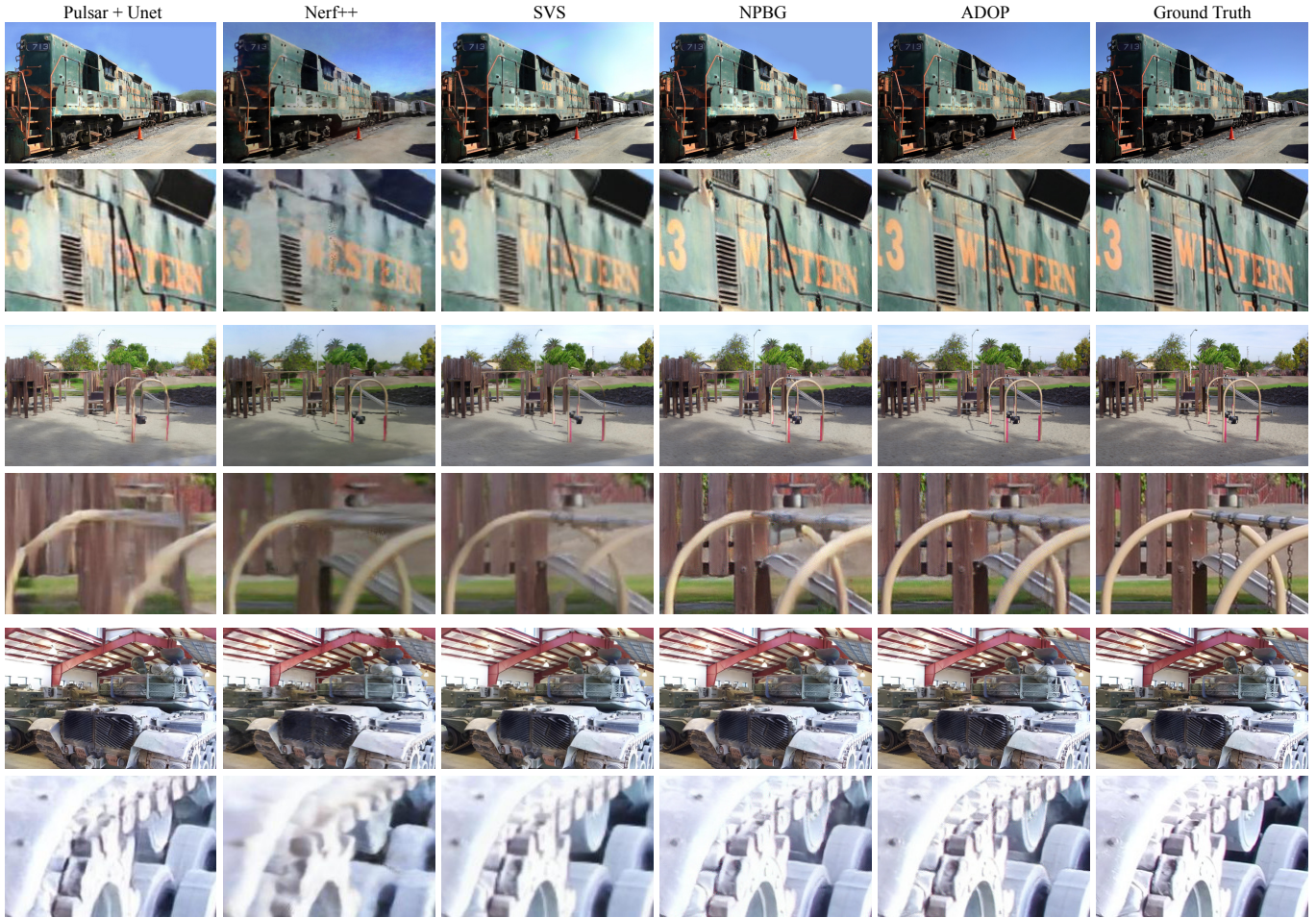


Fig. 10. Comparative results of novel-view synthesis on the *Train*, *Playground*, and *M60* scene. The table below provides a quantitative comparison, in this figure we show images for the methods that perform best. Note that due to memory constraints SVS has been evaluated in half-resolution.

Method	Train			Playground			M60			Lighthouse		
	VGG ↓	LPIPS ↓	PSNR ↑	VGG ↓	LPIPS ↓	PSNR ↑	VGG ↓	LPIPS ↓	PSNR ↑	VGG ↓	LPIPS ↓	PSNR ↑
Synsin + Unet	706.0	0.3853	16.97	521.3	0.3198	21.81	564.3	0.2904	20.16	679.7	0.3655	15.41
Pulsar + Unet	677.9	0.3418	17.78	661.2	0.3849	20.00	508.2	0.2403	21.42	587.1	0.3112	17.82
NRW	817.5	0.4552	14.44	632.8	0.4110	19.47	741.2	0.4476	16.96	709.5	0.3835	14.88
NeRF++	857.5	0.5168	18.04	696.8	0.5292	22.24	700.5	0.4378	23.06	741.2	0.4609	20.06
SVS (half res.)	633.1	0.323	17.43	516.6	0.3462	22.11	461.1	0.2440	23.74	606.5	0.3232	17.12
NPBG	521.9	0.2094	17.66	389.9	0.1816	23.31	380.69	0.1494	24.15	500.0	0.2140	17.54
ADOP	<b>422.6</b>	<b>0.1603</b>	<b>21.62</b>	<b>345.9</b>	<b>0.1594</b>	<b>25.00</b>	<b>342.8</b>	<b>0.1344</b>	<b>25.07</b>	<b>375.1</b>	<b>0.1536</b>	<b>22.44</b>
ADOP w. TR	368.1	0.1438	23.19	318.7	0.1464	25.78	317.7	0.1189	25.84	350.0	0.1439	23.04

Table 4. Quantitative evaluation of novel view synthesis on the four scenes of the tanks and temples dataset. The values in this table represent the mean loss over all test images. ADOP outperforms the other approach with and without test refinement (TR). In the latter, we estimate the exposure value and refine the camera pose of the test images.



Fig. 11. ADOP is able to render fisheye camera systems at high quality.

rendering, which natively supports the camera models, so they have been trained on the original distorted images.

The results (see Fig. 10) show that ADOP is able to produce convincing results on all tested scenes. Compared to the other methods, our renderings show less artifacts as well as preserve color, brightness, and sharpness better. For example, in the close-up view of the playground scene, the metal bars of the swing are most detailed in the ADOP rendering. In the M60 dataset, NPBG has similar visual results, but the quantitative evaluation (in Tab. 4) shows that our method still has the edge. In the last row of Tab. 4 we show the quantitative results of ADOP with test refinement (TR) enabled. TR compensates errors of the initial reconstruction by estimating the exposure value and camera pose of the test frames once training has been completed. This further improves the loss however note that even without TR our approach outperforms the state-of-the-art.

#### 4.9 Fisheye Camera

Our system is able to learn with images originating from fisheye cameras without needing to undistort the projection, resulting in high quality neural fisheye renders (see Fig. 11). The office scene uses a LiDAR and SLAM system for poses and the point cloud, which can be noisy. As presented before, ADOP is able to correct this efficiently.

#### 4.10 View Extrapolation

In Fig. 12 we show reconstructions from a view that is far from the input views, comparing the results of our system with SVS. In general, ADOP generates relatively good results in such cases compared to established methods, although this setup is generally difficult.

#### 4.11 HDR Neural Rendering

When capturing outdoor scenes, it is almost unavoidable to use varying exposure to be able to adapt to the huge range of brightness values. To test the performance of our pipeline on such HDR scenes, we apply it to our *Boat* dataset. The camera was set to auto exposure, all other image related settings, such as aperture, ISO-Speed, and white balance were set constant for all frames. In Fig. 13, four samples from the dataset are shown, underneath the exposure value is plotted for every frame in the dataset. The difference between the smallest and largest EV is 8.7, which corresponds to a factor of  $2^{8.7} = 426.67$ .



Fig. 12. View extrapolation with a large distance to the closest training image.

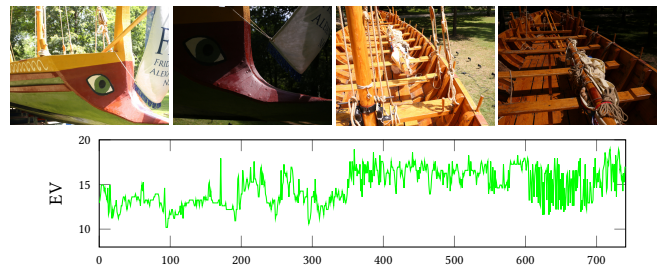


Fig. 13. Sample images of the boat dataset, taken with auto exposure. The exposure value (EV) for each image in the dataset is plotted below the images.

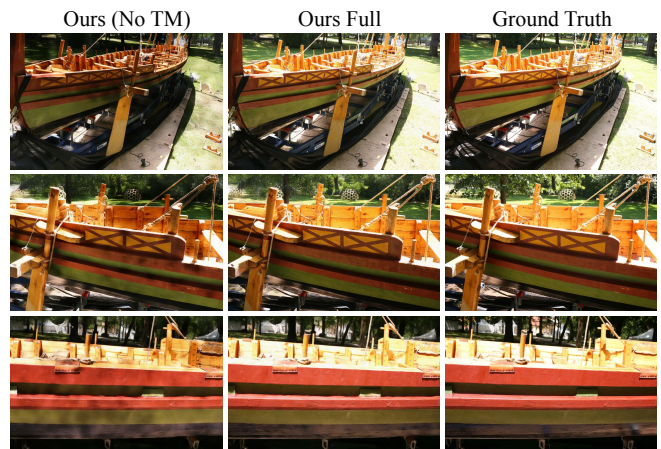


Fig. 14. Novel views synthesized on the boat dataset. Left: no tone mapping and exposure correction results in splotchy artifacts, Center: HDR reconstruction with tone mapping and same exposure as reference photograph. Right: ground truth.

Novel view synthesis results of the Boat scene are shown in Fig. 14. For the images in the left column, uniform exposure was assumed, in the middle column the exposure value used by the tonemapper has been set to the real EV from the EXIF meta data and kept constant during training. Our system is then able to handle the high dynamic range and avoids splotchy artifacts.

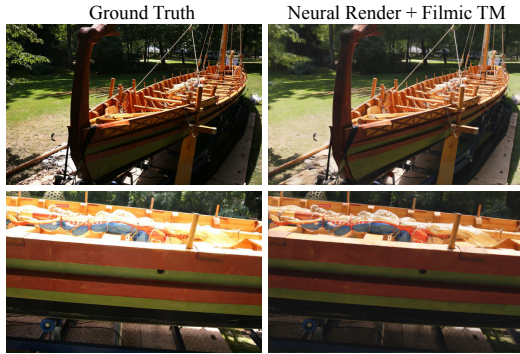


Fig. 15. At inference time, we can replace the learned tone mapper (TM) by a filmic TM, which renders the images in a more natural look.

Additionally, we can replace the learned TM at inference time, for instance by a filmic tone mapper [Hable 2010], that better resembles human perception. The result is shown in Fig. 15. With the filmic tone mapper, the dark areas have significantly more contrast without overexposing the bright wood inside the boat. The filmic TM also slightly reduces color saturation, as such colors look more natural.

## 5 LIMITATIONS

Due to the vast amount of different parameters, the search of suitable hyper parameters is non-trivial. We have to balance learning rates of the texture color, structural parameters, tone mapping settings, and neural network weights. An extensive grid-search was necessary to find viable settings that work well for all of our scenes.

Furthermore, the optimization of point position is not stable for moderate to large learning rates. Our pipeline therefore requires a reasonable initial point cloud, for example, by a multi view stereo system or a LiDAR scanner. We believe that this problem is caused by the gradient approximation during rasterization. It works well for camera model and pose optimization because the spatial gradient of thousands of points are averaged in one optimizer step. For the positional point-gradients however, only a single approximate gradient is used to update its coordinates. A very low learning rate is therefore required to average the point gradient over time.

Finally, due to the one-pixel point rendering, holes appear when the camera is moved too close to an object or the point cloud is very sparse, because the neural network architecture can only fill holes up to a certain size threshold. When the camera moves, also flickering becomes noticeable in such situations—the effect is visible in parts of the accompanying video. Using a deeper neural renderer network helps in these cases, at the price of reduced rendering performance. Future work should be conducted here, for example one could try to dynamically generate new points during magnification that have interpolated neural descriptors or add a temporal component to the neural rendering.

## 6 CONCLUSION

We have presented ADOP, a novel fully differentiable neural point-based rendering pipeline that uses a set of calibrated images and

an estimated point cloud of the scene as input. All stages are differentiable, so we can refine all input parameters to generate an improved output. By also including a photometric sensor model, we can handle input images with varying exposure and generate high dynamic range output.

Our experiments show that, due to the optimized input, we achieve superior rendering quality, especially for novel view synthesis. At the same time, the one-pixel point renderer is very fast. In combination with the fact that the improved consistency in the input allows us to use a simpler and thus faster neural network for reconstruction, we achieve real-time frame rates on a standard GPU, even for complex scenes.

<https://github.com/darglein/ADOP>

## ACKNOWLEDGMENTS

Linus Franke was supported by the Bayerische Forschungsstiftung (Bavarian Research Foundation) AZ-1422-20.

## REFERENCES

- Agisoft. 2021. *Metashape*. <https://www.agisoft.com/>
- Marc Alexa, Markus Gross, Mark Pauly, Hanspeter Pfister, Marc Stamminger, and Matthias Zwicker. 2004. Point-based Computer Graphics. In *ACM SIGGRAPH 2004 Course Notes*. 7–es.
- Kara-Ali Aliev, Artem Sevastopolsky, Maria Kolos, Dmitry Ulyanov, and Victor Lempitsky. 2020. Neural Point-Based Graphics. In *Computer Vision—ECCV 2020: 16th European Conference, Glasgow, UK, August 23–28, 2020, Proceedings, Part XXII* 16. Springer, 696–712.
- Mario Botsch, Alexander Hornung, Matthias Zwicker, and Leif Kobbelt. 2005. High-quality surface splatting on today’s GPUs. In *Proceedings Eurographics/IEEE VGTC Symposium Point-Based Graphics, 2005*. IEEE, 17–141.
- Giang Bui, Truc Le, Brittany Morago, and Ye Duan. 2018. Point-Based Rendering Enhancement via Deep Learning. *The Visual Computer* 34, 6 (2018), 829–841.
- Gaurav Chaurasia, Sylvain Duchene, Olga Sorkine-Hornung, and George Drettakis. 2013. Depth synthesis and local warps for plausible image-based navigation. *ACM Transactions on Graphics (TOG)* 32, 3 (2013), 1–12.
- Wenzheng Chen, Huan Ling, Jun Gao, Edward Smith, Jaakko Lehtinen, Alec Jacobson, and Sanja Fidler. 2019. Learning to Predict 3D Objects With an Interpolation-Based Differentiable Renderer. *Advances in Neural Information Processing Systems* 32 (2019), 9609–9619.
- Peng Dai, Yinda Zhang, Zhuwen Li, Shuaicheng Liu, and Bing Zeng. 2020. Neural Point Cloud Rendering via Multi-Plane Projection. In *Proceedings of the IEEE/CVF Conference on Computer Vision and Pattern Recognition (CVPR)*.
- Paul Debevec, Yizhou Yu, and George Boshokov. 1998. Efficient view-dependent IBR with projective texture-mapping. In *EG Rendering Workshop*, Vol. 4.
- Paul E Debevec and Jitendra Malik. 2008. Recovering High Dynamic Range Radiance Maps from Photographs. In *ACM SIGGRAPH 2008 classes*. 1–10.
- Eric Enderton, Erik Sintorn, Peter Shirley, and David Luebke. 2010. Stochastic Transparency. *IEEE transactions on visualization and computer graphics* 17, 8 (2010), 1036–1047.
- Jakob Engel, Vladlen Koltun, and Daniel Cremers. 2017. Direct Sparse Odometry. *IEEE transactions on pattern analysis and machine intelligence* 40, 3 (2017), 611–625.
- John Flynn, Ivan Neulander, James Philbin, and Noah Snavely. 2016. DeepStereo: Learning to Predict New Views from the World’s Imagery. In *Proceedings of the IEEE conference on computer vision and pattern recognition*. 5515–5524.
- Yaroslav Ganin, Daniil Kononenko, Diana Sungatullina, and Victor Lempitsky. 2016. DeepWarp: Photorealistic Image Resynthesis for Gaze Manipulation. In *European conference on computer vision*. Springer, 311–326.
- Kyle Genova, Forrester Cole, Aaron Maschinot, Aaron Sarna, Daniel Vlasic, and William T Freeman. 2018. Unsupervised Training for 3D Morphable Model Regression. In *Proceedings of the IEEE Conference on Computer Vision and Pattern Recognition*. 8377–8386.
- Daniel B Goldman. 2010. Vignette and Exposure Calibration and Compensation. *IEEE transactions on pattern analysis and machine intelligence* 32, 12 (2010), 2276–2288.
- Michael D Grossberg and Shree K Nayar. 2003. Determining the Camera Response from Images: What is Knowable? *IEEE Transactions on pattern analysis and machine intelligence* 25, 11 (2003), 1455–1467.
- Jeffrey P Grossman and William J Dally. 1998. Point Sample Rendering. In *Eurographics Workshop on Rendering Techniques*. Springer, 181–192.

- Christian Günther, Thomas Kanzok, Lars Linsen, and Paul Rosenthal. 2013. A GPGPU-based pipeline for accelerated rendering of point clouds. (2013).
- John Hable. 2010. Filmic Tonemapping for Real-time Rendering. In *Siggraph 2010 Color Course*.
- Zhizhong Han, Chao Chen, Yu-Shen Liu, and Matthias Zwicker. 2020. DRWR: A Differentiable Renderer without Rendering for Unsupervised 3D Structure Learning from Silhouette Images. In *International Conference on Machine Learning 2020*.
- Peter Hedman, Julien Philip, True Price, Jan-Michael Frahm, George Drettakis, and Gabriel Brostow. 2018. Deep Blending for Free-Viewpoint Image-Based Rendering. *ACM Transactions on Graphics (TOG)* 37, 6 (2018), 1–15.
- Philipp Henzler, Niloy J Mitra, and Tobias Ritschel. 2019. Escaping Plato’s Cave: 3D Shape From Adversarial Rendering. In *Proceedings of the IEEE/CVF International Conference on Computer Vision*. 9984–9993.
- Xin Huang, Qi Zhang, Feng Ying, Hongdong Li, Xuan Wang, and Qing Wang. 2021. HDR-NeRF: High Dynamic Range Neural Radiance Fields. *arXiv preprint arXiv:2111.14451* (2021).
- Eldar Insafutdinov and Alexey Dosovitskiy. 2018. Unsupervised learning of shape and pose with differentiable point clouds. In *Proceedings of the 32nd International Conference on Neural Information Processing Systems*. 2807–2817.
- Yoonwoo Jeong, Seokjun Ahn, Christopher Choy, Anima Anandkumar, Minsu Cho, and Jaesik Park. 2021. Self-Calibrating Neural Radiance Fields. In *Proceedings of the IEEE/CVF International Conference on Computer Vision*. 5846–5854.
- Yangqing Jia, Evan Shelhamer, Jeff Donahue, Sergey Karayev, Jonathan Long, Ross Girshick, Sergio Guadarrama, and Trevor Darrell. 2014. Caffe: Convolutional architecture for fast feature embedding. In *Proceedings of the 22nd ACM international conference on Multimedia*. 675–678.
- Yue Jiang, Dantong Ji, Zhizhong Han, and Matthias Zwicker. 2020. SDFDiff: Differentiable Rendering of Signed Distance Fields for 3D Shape Optimization. In *Proceedings of the IEEE/CVF Conference on Computer Vision and Pattern Recognition*. 1251–1261.
- Justin Johnson, Alexandre Alahi, and Li Fei-Fei. 2016. Perceptual Losses for Real-Time Style Transfer and Super-Resolution. In *European conference on computer vision*. Springer, 694–711.
- Hiroharu Kato, Deniz Beker, Mihai Morariu, Takahiro Ando, Toru Matsuoka, Wadim Kehl, and Adrien Gaidon. 2020. Differentiable Rendering: A Survey. *arXiv preprint arXiv:2006.12057* (2020).
- Hiroharu Kato and Tatsuya Harada. 2019. Learning View Priors for Single-View 3D Reconstruction. In *Proceedings of the IEEE/CVF Conference on Computer Vision and Pattern Recognition*. 9778–9787.
- Hiroharu Kato, Yoshitaka Ushiku, and Tatsuya Harada. 2018. Neural 3D Mesh Renderer. In *Proceedings of the IEEE conference on computer vision and pattern recognition*. 3907–3916.
- Diederik P. Kingma and Jimmy Ba. 2015. Adam: A Method for Stochastic Optimization. In *3rd International Conference on Learning Representations, ICLR 2015, San Diego, CA, USA, May 7-9, 2015, Conference Track Proceedings*, Yoshua Bengio and Yann LeCun (Eds.). <http://arxiv.org/abs/1412.6980>
- Arno Knapitsch, Jaesik Park, Qian-Yi Zhou, and Vladlen Koltun. 2017. Tanks and Temples: Benchmarking Large-Scale Scene Reconstruction. *ACM Transactions on Graphics (ToG)* 36, 4 (2017), 1–13.
- Leif Kobbelt and Mario Botsch. 2004. A Survey of Point-Based Techniques in Computer Graphics. *Computers & Graphics* 28, 6 (2004), 801–814.
- Georgios Kopanas, Julien Philip, Thomas Leimkühler, and George Drettakis. 2021. Point-Based Neural Rendering with Per-View Optimization. In *Computer Graphics Forum*, Vol. 40. Wiley Online Library, 29–43.
- Christoph Lassner and Michael Zollhöfer. 2021. Pulsar: Efficient Sphere-Based Neural Rendering. In *Proceedings of the IEEE/CVF Conference on Computer Vision and Pattern Recognition (CVPR)*. 1440–1449.
- Hoang-An Le, Thomas Mensink, Partha Das, and Theo Gevers. 2020. Novel View Synthesis from Single Images via Point Cloud Transformation. *arXiv preprint arXiv:2009.08321* (2020).
- Marc Levoy and Turner Whitted. 1985. *The Use of Points as a Display Primitive*. Citeseer.
- Chen-Hsuan Lin, Chen Kong, and Simon Lucey. 2018. Learning Efficient Point Cloud Generation for Dense 3D Object Reconstruction. In *proceedings of the AAAI Conference on Artificial Intelligence*, Vol. 32.
- Chen-Hsuan Lin, Wei-Chiu Ma, Antonio Torralba, and Simon Lucey. 2021. BARF: Bundle-Adjusting Neural Radiance Fields. In *Proceedings of the IEEE/CVF International Conference on Computer Vision*. 5741–5751.
- Shichen Liu, Tianye Li, Weikai Chen, and Hao Li. 2019a. Soft Rasterizer: A Differentiable Renderer for Image-based 3D Reasoning. In *Proceedings of the IEEE/CVF International Conference on Computer Vision*. 7708–7717.
- Shichen Liu, Shunsuke Saito, Weikai Chen, and Hao Li. 2019b. Learning to Infer Implicit Surfaces without 3D Supervision. *Advances in Neural Information Processing Systems* 32 (2019), 8295–8306.
- Shaohui Liu, Yinda Zhang, Songyou Peng, Boxin Shi, Marc Pollefeys, and Zhaopeng Cui. 2020. DIST: Rendering Deep Implicit Signed Distance Function with Differentiable Sphere Tracing. In *Proceedings of the IEEE/CVF Conference on Computer Vision and Pattern Recognition*. 2019–2028.
- Stephen Lombardi, Tomas Simon, Jason Saragih, Gabriel Schwartz, Andreas Lehrmann, and Yaser Sheikh. 2019. Neural Volumes: Learning Dynamic Renderable Volumes From Images. *ACM Transactions on Graphics (TOG)* 38, 4 (2019), 1–14.
- Matthew M Loper and Michael J Black. 2014. OpenDR: An approximate differentiable renderer. In *European Conference on Computer Vision*. Springer, 154–169.
- Ricardo Marroquim, Martin Kraus, and Paulo Roma Cavalcanti. 2007. Efficient Point-Based Rendering Using Image Reconstruction. In *PBG@ Eurographics*. 101–108.
- Ricardo Martin-Brualla, Noha Radwan, Mehdi SM Sajjadi, Jonathan T Barron, Alexey Dosovitskiy, and Daniel Duckworth. 2021. NeRF in the Wild: Neural Radiance Fields for Unconstrained Photo Collections. In *Proceedings of the IEEE/CVF Conference on Computer Vision and Pattern Recognition*. 7210–7219.
- Lars Mescheder, Michael Oechsle, Michael Niemeyer, Sebastian Nowozin, and Andreas Geiger. 2019. Occupancy Networks: Learning 3D Reconstruction in Function Space. In *Proceedings of the IEEE/CVF Conference on Computer Vision and Pattern Recognition*. 4460–4470.
- Moustafa Meshry, Dan B Goldman, Sameh Khamis, Hugues Hoppe, Rohit Pandey, Noah Snavely, and Ricardo Martin-Brualla. 2019. Neural re-rendering in the wild. In *Proceedings of the IEEE/CVF Conference on Computer Vision and Pattern Recognition*. 6878–6887.
- Ben Mildenhall, Peter Hedman, Ricardo Martin-Brualla, Pratul Srinivasan, and Jonathan T Barron. 2021. NeRF in the Dark: High Dynamic Range View Synthesis from Noisy Raw Images. *arXiv preprint arXiv:2111.13679* (2021).
- Ben Mildenhall, Pratul P Srinivasan, Rodrigo Ortiz-Cayon, Nima Khademi Kalantari, Ravi Ramamoorthi, Ren Ng, and Abhishek Kar. 2019. Local Light Field Fusion: Practical View Synthesis With Prescriptive Sampling Guidelines. *ACM Transactions on Graphics (TOG)* 38, 4 (2019), 1–14.
- Ben Mildenhall, Pratul P Srinivasan, Matthew Tancik, Jonathan T Barron, Ravi Ramamoorthi, and Ren Ng. 2020. NeRF: Representing Scenes as Neural Radiance Fields for View Synthesis. In *European conference on computer vision*. Springer, 405–421.
- Raul Mur-Artal and Juan D Tardós. 2017. ORB-SLAM2: An open-source slam system for monocular, stereo, and rgb-d cameras. *IEEE transactions on robotics* 33, 5 (2017), 1255–1262.
- Thu Nguyen-Phuoc, Chuan Li, Stephen Balaban, and Yong-Liang Yang. 2018. RenderNet: A deep convolutional network for differentiable rendering from 3D shapes. In *Proceedings of the 32nd International Conference on Neural Information Processing Systems*. 7902–7912.
- Michael Niemeyer, Lars Mescheder, Michael Oechsle, and Andreas Geiger. 2020. Differentiable Volumetric Rendering: Learning Implicit 3D Representations without 3D Supervision. In *Proceedings of the IEEE/CVF Conference on Computer Vision and Pattern Recognition*. 3504–3515.
- Jeong Joon Park, Peter Florence, Julian Straub, Richard Newcombe, and Steven Lovegrove. 2019. DeepSDF: Learning Continuous Signed Distance Functions for Shape Representation. In *Proceedings of the IEEE/CVF Conference on Computer Vision and Pattern Recognition*. 165–174.
- Adam Paszke, Sam Gross, Francisco Massa, Adam Lerer, James Bradbury, Gregory Chanan, Trevor Killeen, Zeming Lin, Natalia Gimelshein, Luca Antiga, et al. 2019. PyTorch: An imperative style, high-performance deep learning library. *Advances in neural information processing systems* 32 (2019), 8026–8037.
- Hanspeter Pfister, Matthias Zwicker, Jeroen Van Baar, and Markus Gross. 2000. Surfels: Surface elements as rendering primitives. In *Proceedings of the 27th annual conference on Computer graphics and interactive techniques*. 335–342.
- Ruggero Pintus, Enrico Gobbetti, and Marco Agus. 2011. Real-time rendering of massive unstructured raw point clouds using screen-space operators. In *Proceedings of the 12th International conference on Virtual Reality, Archaeology and Cultural Heritage*. 105–112.
- Francesco Pittaluga, Sanjeev J. Koppal, Sing Bing Kang, and Sudipta N. Sinha. 2019. Revealing Scenes by Inverting Structure From Motion Reconstructions. In *Proceedings of the IEEE/CVF Conference on Computer Vision and Pattern Recognition (CVPR)*.
- Reinhold Preiner, Stefan Jeschke, and Michael Wimmer. 2012. Auto Splats: Dynamic Point Cloud Visualization on the GPU. In *EGPGV@ Eurographics*. 139–148.
- Nikhila Ravi, Jeremy Reizenstein, David Novotny, Taylor Gordon, Wan-Yen Lo, Justin Johnson, and Georgia Gkioxari. 2020. Accelerating 3D Deep Learning with PyTorch3D. *arXiv preprint arXiv:2007.08501* (2020).
- Helge Rhodin, Nadia Robertini, Christian Richardt, Hans-Peter Seidel, and Christian Theobalt. 2015. A Versatile Scene Model With Differentiable Visibility Applied to Generative Pose Estimation. In *Proceedings of the IEEE International Conference on Computer Vision*. 765–773.
- Gernot Riegler and Vladlen Koltun. 2020. Free View Synthesis. In *European Conference on Computer Vision*. Springer, 623–640.
- Gernot Riegler and Vladlen Koltun. 2021. Stable View Synthesis. In *Proceedings of the IEEE/CVF Conference on Computer Vision and Pattern Recognition*. 12216–12225.
- Paul Rosenthal and Lars Linsen. 2008. Image-space point cloud rendering. In *Proceedings of Computer Graphics International*. Citeseer, 136–143.
- Darius Rückert and Marc Stamminger. 2021. Snake-SLAM: Efficient Global Visual Inertial SLAM using Decoupled Nonlinear Optimization. In *2021 International Conference on Unmanned Aircraft Systems (ICUAS)*. IEEE, 219–228.

- Johannes L Schönberger and Jan-Michael Frahm. 2016. Structure-from-motion revisited. In *Proceedings of the IEEE conference on computer vision and pattern recognition*. 4104–4113.
- Markus Schütz, Bernhard Kerbl, and Michael Wimmer. 2021. Rendering Point Clouds with Compute Shaders and Vertex Order Optimization. *Computer Graphics Forum* (2021). <https://doi.org/10.1111/cgf.14345>
- Dave Shreiner, Bill The Khronos OpenGL ARB Working Group, et al. 2009. *OpenGL programming guide: the official guide to learning OpenGL, versions 3.0 and 3.1*. Pearson Education.
- Harry Shum and Sing Bing Kang. 2000. Review of image-based rendering techniques. In *Visual Communications and Image Processing 2000*, Vol. 4067. International Society for Optics and Photonics, 2–13.
- Vincent Sitzmann, Julien Martel, Alexander Bergman, David Lindell, and Gordon Wetzstein. 2020. Implicit neural representations with periodic activation functions. *Advances in Neural Information Processing Systems* 33 (2020).
- Vincent Sitzmann, Justus Thies, Felix Heide, Matthias Nießner, Gordon Wetzstein, and Michael Zollhofer. 2019. DeepVoxels: Learning Persistent 3D Feature Embeddings. In *Proceedings of the IEEE/CVF Conference on Computer Vision and Pattern Recognition*. 2437–2446.
- Zhenbo Song, Wayne Chen, Dylan Campbell, and Hongdong Li. 2020. Deep Novel View Synthesis from Colored 3D Point Clouds. In *European Conference on Computer Vision*. Springer, 1–17.
- Pratul P Srinivasan, Richard Tucker, Jonathan T Barron, Ravi Ramamoorthi, Ren Ng, and Noah Snavely. 2019. Pushing the Boundaries of View Extrapolation With Multiplane Images. In *Proceedings of the IEEE/CVF Conference on Computer Vision and Pattern Recognition*. 175–184.
- Matthew Tancik, Vincent Casser, Xinchun Yan, Sabeek Pradhan, Ben Mildenhall, Pratul P Srinivasan, Jonathan T Barron, and Henrik Kretzschmar. 2022. Block-NeRF: Scalable Large Scene Neural View Synthesis. *arXiv preprint arXiv:2202.05263* (2022).
- Ayush Tewari, Ohad Fried, Justus Thies, Vincent Sitzmann, Stephen Lombardi, Kalyan Sunkavalli, Ricardo Martin-Brualla, Tomas Simon, Jason Saragih, Matthias Nießner, et al. 2020. State of the Art on Neural Rendering. In *Computer Graphics Forum*, Vol. 39. Wiley Online Library, 701–727.
- Justus Thies, Michael Zollhofer, and Matthias Nießner. 2019. Deferred Neural Rendering: Image Synthesis using Neural Textures. *ACM Transactions on Graphics (TOG)* 38, 4 (2019), 1–12.
- Justus Thies, Michael Zollhofer, Christian Theobalt, Marc Stamminger, and Matthias Nießner. 2020. Image-guided neural object rendering. In *8th International Conference on Learning Representations*. OpenReview. net.
- Richard Tucker and Noah Snavely. 2020. Single-View View Synthesis With Multiplane Images. In *Proceedings of the IEEE/CVF Conference on Computer Vision and Pattern Recognition*. 551–560.
- Shubham Tulsiani, Tinghui Zhou, Alexei A Efros, and Jitendra Malik. 2017. Multi-View Supervision for Single-View Reconstruction via Differentiable Ray Consistency. In *Proceedings of the IEEE conference on computer vision and pattern recognition*. 2626–2634.
- Olivia Wiles, Georgia Gkioxari, Richard Szeliski, and Justin Johnson. 2020. SynSin: End-to-end View Synthesis from a Single Image. In *Proceedings of the IEEE/CVF Conference on Computer Vision and Pattern Recognition*. 7467–7477.
- Bing Xu, Naiyan Wang, Tianqi Chen, and Mu Li. 2015. Empirical Evaluation of Rectified Activations in Convolutional Network. *arXiv preprint arXiv:1505.00853* (2015).
- Zhenpei Yang, Yuning Chai, Dragomir Anguelov, Yin Zhou, Pei Sun, Dumitru Erhan, Sean Rafferty, and Henrik Kretzschmar. 2020. SurfelGAN: Synthesizing Realistic Sensor Data for Autonomous Driving. In *Proceedings of the IEEE/CVF Conference on Computer Vision and Pattern Recognition (CVPR)*.
- Wang Yifan, Felice Serena, Shihao Wu, Cengiz Öztireli, and Olga Sorkine-Hornung. 2019. Differentiable Surface Splatting for Point-based Geometry Processing. *ACM Transactions on Graphics (TOG)* 38, 6 (2019), 1–14.
- Alex Yu, Vickie Ye, Matthew Tancik, and Angjoo Kanazawa. 2021. pixelNeRF: Neural Radiance Fields From One or Few Images. In *Proceedings of the IEEE/CVF Conference on Computer Vision and Pattern Recognition*. 4578–4587.
- Jiahui Yu, Zhe Lin, Jimei Yang, Xiaohui Shen, Xin Lu, and Thomas S Huang. 2019. Free-Form Image Inpainting with Gated Convolution. In *Proceedings of the IEEE/CVF International Conference on Computer Vision*. 4471–4480.
- Sergey Zakharov, Wadim Kehl, Arjun Bhargava, and Adrien Gaidon. 2020. Autolabeling 3D Objects with Differentiable Rendering of SDF Shape Priors. In *Proceedings of the IEEE/CVF Conference on Computer Vision and Pattern Recognition*. 12224–12233.
- Kai Zhang, Gernot Riegler, Noah Snavely, and Vladlen Koltun. 2020. NeRF++: Analyzing and Improving Neural Radiance Fields. *arXiv preprint arXiv:2010.07492* (2020).
- Richard Zhang, Phillip Isola, Alexei A Efros, Eli Shechtman, and Oliver Wang. 2018. The Unreasonable Effectiveness of Deep Features as a Perceptual Metric. In *CVPR*.
- Tinghui Zhou, Richard Tucker, John Flynn, Graham Fyfe, and Noah Snavely. 2018. Stereo Magnification: Learning View Synthesis Using Multiplane Images. *ACM Transactions on Graphics (TOG)* 37, 4 (2018), 1–12.
- Tinghui Zhou, Shubham Tulsiani, Weilun Sun, Jitendra Malik, and Alexei A Efros. 2016. View Synthesis by Appearance Flow. In *European conference on computer vision*. Springer, 286–301.
- Jun-Yan Zhu, Zhoutong Zhang, Chengkai Zhang, Jiajun Wu, Antonio Torralba, Josh Tenenbaum, and Bill Freeman. 2018. Visual Object Networks: Image Generation with Disentangled 3D Representations. *Advances in Neural Information Processing Systems* 31 (2018), 118–129.
- Matthias Zwicker, Hanspeter Pfister, Jeroen Van Baar, and Markus Gross. 2001. Surface Splatting. In *Proceedings of the 28th annual conference on Computer graphics and interactive techniques*. 371–378.

## A IMAGE TO POINT CLOUD ALIGNMENT

Another application of our differentiable rendering pipeline is the alignment of camera images to point-clouds that were reconstructed by external devices. (Anonymous) provided us a dataset captured by the (Anonymous) mobile scanning platform. This platform consists of a high performance LiDAR scanner and four  $5472 \times 3648$  pixel fisheye cameras. Their reconstruction software is able to combine multiple laser scans into a consistent point cloud and provides camera pose estimates for panorama generation and point cloud coloring. However, the image to point cloud registration is not perfect. Small errors during the SLAM-based tracking and vibrations due to the hand-held operation result in pose errors in the scale of millimeters. If we then use these poses for precise operation, such as reprojecting the color of neighboring source images into a target view, small ghosting artifacts can be observed (see Figure 16 center row). We train our neural rendering pipeline on this office dataset, which is composed of 688 images and 73M points, to synthesize all captured views. During training, our system also optimizes the camera pose of each frame. The refined poses are then used to reproject the colors into the same target frame as before (see Figure 16 bottom row). It can be seen that the ghosting artifacts are mostly eliminated and the synthesized image is a lot sharper. This experiment shows that the proposed method is able to perform pixel-perfect alignment of fisheye camera images to a point cloud of a LiDAR scanner. To our knowledge, no other available differentiable renderer can fulfill this task, as they assume a pinhole camera model or are not able to handle a point cloud with 73M points.

## B RUNTIME PERFORMANCE

Runtime performance has been a limiting factor for differentiable rendering systems in the past [Kato et al. 2020]. Most software rasterization techniques exceed the 100 ms barrier even for small scenes and render resolutions [Lassner and Zollhofer 2021]. This limits their usefulness in real-world applications such as 3D reconstruction from high-resolution photographs. Currently, the two most performant differentiable rendering methods that are able to process point-cloud data are Synsin [Wiles et al. 2020] and Pulsar [Lassner and Zollhofer 2021]. Synsin, which is the default point render engine of PyTorch3D [Ravi et al. 2020], splats each point to a disk and blends the  $K$  nearest points of each pixel into the output image. Pulsar converts each point to sphere and blends them with a similar approach as Soft Rasterizer [Liu et al. 2019a]. Both methods are fully differentiable, meaning that the point position and color can be optimized during rendering.

Table 5 shows the measured GPU frame-time for Synsin, Pulsar, our approach, and OpenGL’s default point rendering with `GL_POINTS`. These timings only include the rasterization itself without the neural network and tonemapper described in the previous sections. For

	Geometry	# Layers	Forward	Backward	Forward	Backward	Forward	Backward	Forward	Backward
Synsin	Disc Splats	1	856.63	14.14	1692.63	17.15	3859.1	31.16	7342.05	25.73
Pulsar ( $r = 0.005$ )	Spheres	1	31.20	3.62	59.69	6.97	129.60	15.06	216.07	16.32
Pulsar ( $r = 0.02$ )	Spheres	1	36.81	3.02	70.78	5.80	152.89	12.53	263.59	14.91
Pulsar ( $r = 0.05$ )	Spheres	1	53.29	3.09	102.48	5.95	221.35	12.85	379.06	15.19
GL_POINTS	1-Pixel Points	1	0.3	×	0.54	×	1.09	×	1.85	×
Ours	1-Pixel Points	1	0.83	0.62	1.09	0.78	1.59	1.39	2.33	2.34
Ours	1-Pixel Points	4	1.4	0.77	1.82	1.24	2.52	1.74	3.65	2.8
<b>Ours + Stoc. Disc.</b>	<b>1-Pixel Points</b>	<b>4</b>	<b>1.28</b>	<b>0.66</b>	<b>1.66</b>	<b>1.07</b>	<b>2.15</b>	<b>1.66</b>	<b>3.08</b>	<b>2.64</b>
	# Points		1,348,406		2,570,810		5,400,615		10,283,243	

Table 5. Forward and backward render-time in milliseconds of a  $1920 \times 1080$  image on a RTX 2080 Ti. In comparison to other differentiable renderers, our approach is around two magnitudes more efficient. The highlighted row is our approach with stochastic point discarding (see Section 3.1) that we use for scene refinement and novel-view synthesis.

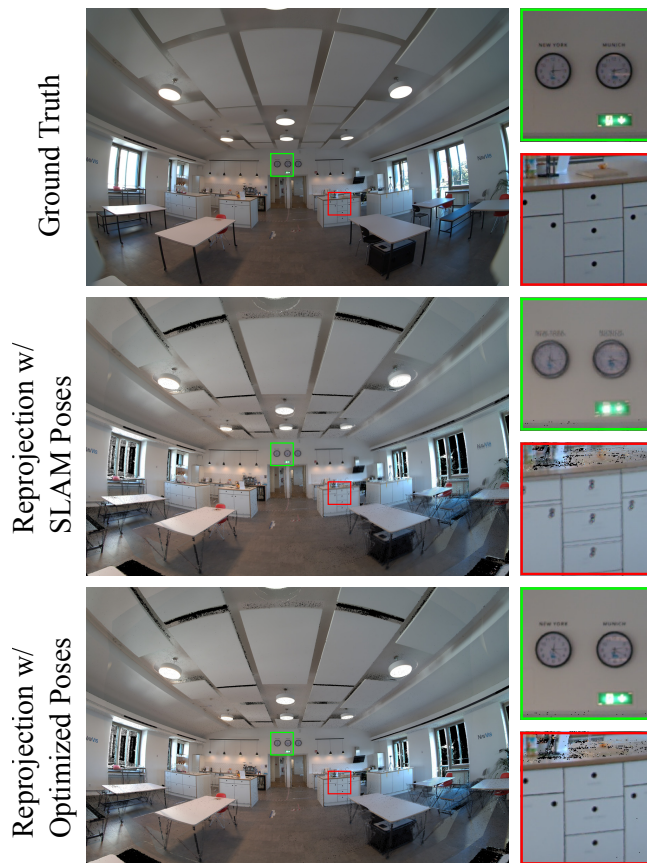


Fig. 16. The initial camera pose estimates of the SLAM-System are slightly misaligned w.r.t. the LiDAR point cloud. Reprojecting the pixel color of several source views into a target view produces ghosting artifacts (center row). Our system is able to optimize the camera poses resulting in almost pixel perfect reprojections (bottom row).

our method, we also include the rendering time of four layers in different resolutions. This is a more fair comparison to the other methods because all four layers are required for the neural rendering network. The output of Synsin and Pulsar is more complete and

therefore a single layer can already be successfully used. The right most columns of Table 5 show the forward and backward render time of a  $1920 \times 1080$  image for a point cloud with around 10M points. Both Synsin and Pulsar are not real-time capable at such dimensions with forward timings of 7342 ms and 209 ms respectively. Our approach takes two magnitudes less time than Pulsar with a combined rendering time of 3.65 ms for all four layers. This result is expected though because previous work has shown that software one-pixel point rendering can outperform hardware rasterization techniques [Schütz et al. 2021]. Point splatting and sphere rendering is inherently more complex because each point effects multiple output pixels.

If we enable stochastic discarding (see Section 3.1), the rendering performance is further increased. The largest gains are achieved for multi-resolution rendering of large point clouds. For example, generating a multi-layer image of the cloud with 10.4M points takes 19% less time with our stochastic discarding approach. However, if only a single image layer is required, the speedup due to stochastic discarding reduces to 3%, as points are only discarded if they fill less than one pixel in the output image. The pixels inside the low resolution layers are much larger and therefore more points are discarded. In comparison to native GL\_POINTS rendering, our approach is only slightly slower (by about 26%). This is an impressive result, because we have implemented a three-pass blending approach with fuzzy depth-test as described in Section 3.1. The GL\_POINTS reference implementation in Table 5 uses a single pass without blending and standard GL\_LESS depth test.